Evidence for weak seismic attenuation in Mars' deep mantle

Jiaqi Li [1] ✉, Junlin Hua [2,3,4], Thomas P. Ferrand [5,6,7], Laurent Pou[8], Quancheng Huang [9], Laetitia Allibert[10,11], Haoran Meng [12], Henri Samuel [13], Zhicheng Jing [12], Wenzhong Wang [2,3,4], Ting Yang [12] & Tong Zhou [1,14]

The present-day distribution of surface and subsurface water on Mars reflects a complex history of exchange between the planet's surface and interior since its formation. Constraining the water content of the deep mantle is essential for estimating the planet's total water budget and understanding its long-term geologic and hydrologic evolution. Yet, the abundance of water at depth remains loosely constrained. Here, we analyze seismic data from global tectonic marsquakes and meteorite impacts recorded by the InSight mission, and identify evidence for weaker attenuation in Mars' deep mantle (500–1500 km), in contrast to Earth. This low attenuation likely reflects fundamental differences in mantle properties between the two planets, including water content, grain size, oxygen fugacity, and/ or temperature. Isolating the role of water from other parameters is key to quantifying Mars' deep water reservoir and provides new constraints on the volatile inventory and interior evolution of the red planet.

The search for environments capable of sustaining life has long been a fundamental driver in space exploration. At the heart of this quest is the presence of liquid water. Mars, having accreted material at greater distances from the Sun, was traditionally thought to be richer in water than Earth[1]. However, recent studies challenge this view, suggesting that the building blocks of Earth and Mars may share a greater similarity (up to 80–93%) than previously assumed[2]. In addition to uncertainties about Mars' initial water content, the processes driving its subsequent evolution remain poorly understood. Atmospheric erosion, the cessation of its magnetic dynamo, and crustal hydration are believed to have played key roles in the disappearance of surface water[3–8]. Meanwhile, surface water may be replenished through magmatic degassing processes[9–11]. However, the quantitative influence of these mechanisms remains largely unconstrained. Clarifying how and where water is currently stored within Mars' interior, particularly in comparison to Earth, is critical to understanding the formation, evolution, and habitability of Mars.

On the Martian surface, evidence of water, primarily in solid form, has been documented in the polar regions and at high latitudes[12–14]. The detections of hydrous minerals like serpentine[15–17] provide evidence of past aqueous alteration in olivine-rich rocks. For the present-day water distribution, InSight seismic data[18] present conflicting interpretations for the equatorial regions: some studies propose the existence of liquid water reservoirs in the mid-crust (10–20 km depth) beneath the landing site[19], while others find the crust to be essentially dry with negligible volatile content[20,21].

In the deep mantle, Earth's mantle transition zone is recognized as a potential reservoir for water[22,23], likely facilitated by rehydration through subduction since the onset of plate tectonics[24]. By contrast, Mars's deeper mantle is estimated to have a water storage capacity equivalent to $\simeq 9$ km in Global Equivalent Layer[25], but its actual water abundance remains only loosely constrained. This pivotal gap on Mars leaves the presence of deep-water reservoirs and their role in shaping the planet's geological evolution and habitability an open question.

Intrinsic attenuation (hereafter referred to as attenuation), the rate at which energy dissipates within a planet, reflects key factors of its interior, such as composition, temperature, mineral grain size, and the presence of

[1]SKLab-DeepMinE, MOEKLab-OBCE, School of Earth and Space Sciences, Peking University, Beijing, China. [2]Laboratory of Seismology and Physics of Earth's Interior, School of Earth and Space Sciences, University of Science and Technology of China, Hefei, China. [3]State Key Laboratory of Precision Geodesy, University of Science and Technology of China, Hefei, Anhui, China. [4]Mengcheng National Geophysical Observatory, University of Science and Technology of China, Mengcheng, Anhui, China. [5]Institute of Geological Sciences, Freie Universität Berlin, Berlin, Germany. [6]Institut Langevin, ESPCI Paris, CNRS, PSL University, Paris, France. [7]Laboratoire de Géologie de l'Ecole de Normale Supérieure, CNRS UMR 8538, PSL Research University, Paris, France. [8]ArianeGroup, Les Mureaux, France. [9]Geophysical R&D Institute, China Oilfield Service Ltd, Tianjin, China. [10]Museum für Naturkunde – Leibniz Institute for Evolution and Biodiversity Science, Berlin, Germany. [11]Department of Earth and Environmental Sciences, KU Leuven, Leuven, Belgium. [12]Southern University of Science and Technology, Shenzhen, China. [13]CNRS, Institut de physique du globe de Paris, Université Paris Cité, Paris, France. [14]Institute of Energy, Peking University, Beijing, China. ✉e-mail: JLI@pku.edu.cn

fluids[26–30]. On Earth, attenuation has been extensively studied for over a century using seismology[31,32]. On Mars, prior to the successful deployment of a seismometer, Mars' attenuation can be inferred from tidal constraints. The tidal forces of Phobos, Mars's largest and closest moon, induce measurable secular acceleration on Mars due to the planet's anelastic properties, providing a basis for estimating the attenuation of Mars[33–35]. However, the bulk attenuation derived from tides offers an integrated view of the entire planet but cannot reveal the radial attenuation profiles within Mars's crust, upper mantle, and transition zone (Fig. 1b).

To infer depth-dependent attenuation profiles, such as shear quality factor $Q_\mu(r)$ (inversely proportional to attenuation, where r is the radius), from the bulk degree-2 global (bulk) quality factor (Q_2) is challenging. This conversion depends on various assumptions about rheology, temperature, grain size, and other factors[36–38]. For instance, the bulk Q_2 of 93.0 ± 8.4 derived from Phobos' tidal constraints[38–40] can be explained by multiple models (Fig. 2a), each representing distinct internal conditions (Supplementary Table 1).

Seismic ruptures have now been identified on every rocky body equipped with a seismometer, i.e., Earth, the Moon, and Mars[41–43]. In this study, we use seismic data from the InSight mission, which records global tectonic marsquakes and meteorite impacts[43–45]. While previous Martian seismological studies have primarily focused on regional events with seismic waves confined to the top ~ 200 km of the lithosphere, our study emphasizes distant events where seismic energy traverses the entire Martian mantle to depths of up to 1500 km (Fig. 1). By combining these seismic constraints with tidal data from Phobos, we aim to derive depth-dependent attenuation profiles for Mars. This integrated approach will enhance our ability to elucidate Mars's internal structures, water content, and geological history. Furthermore, by comparing Mars and Earth, we can gain a deeper understanding of the formation, evolution, dynamics, and potential habitability of rocky planets in our solar system.

Results

The InSight SEIS seismometer[46] has recorded both tectonic marsquakes and meteorite impacts, with seismic energy propagating through the entire Martian mantle to depths of up to 1500 km (Fig. 1). These seismic waves typically have periods of around 1 s, in contrast to the much longer tidal periods, which span several hours. Because attenuation is inherently

dependent on frequency (see "Methods"), seismic measurements complement tidal observations and enable the derivation of depth-dependent attenuation profiles for Mars.

For instance, although previously proposed models appear similar at Phobos' tidal period (5 h 33 min), they diverge significantly at 1 s. At this seismic period, these models cluster into two distinct groups: the "strong attenuation" group and the "weak attenuation" group (Fig. 2b). Within the mantle depth range of 150–1500 km (2–20 GPa for Mars), the "strong attenuation" group is characterized by low $Q_P(r)$ values (~300), whereas the "weak attenuation" group displays much higher $Q_P(r)$ values (700–9000). To distinguish between these two groups—and thereby differentiate among various rheological and compositional scenarios, such as dry versus wet conditions within Mars' deep interior—additional constraints at shorter periods are essential.

To estimate short-period attenuation, one approach is to analyze the decay of seismic energy with frequency. On Earth, dense seismic networks enabled comprehensive attenuation estimates in one-, three-, and even four-dimensional contexts, including real-time monitoring[29,47]. In contrast, Mars was equipped with only a single seismometer, posing challenges for accurately estimating the attenuation along seismic paths. These challenges stem from the tradeoffs among intrinsic attenuation, scattering, and the seismic source, all contributing to the observed energy loss observed in seismic waves[48]. To address this, we propose a novel approach that prioritizes estimating the maximum limit of intrinsic attenuation over precise values (see "Methods" and Supplementary Table 2). By deliberately excluding the effects of source and scattering, our method purposefully overestimates intrinsic attenuation by attributing the energy loss entirely to it.

This approach establishes robust upper bounds for Martian intrinsic attenuation (i.e., lower bounds for the quality factor $Q(r)$), particularly at depth ranges where reliable measurements were previously unavailable. We divided Mars' interior into four regions and assumed constant $Q(r)$ values within each layer (see "Methods" and Fig. 2b). These regions include the upper lithosphere (0–150 km), lower lithosphere (150–500 km), upper mantle (500–1000 km), and mantle transition zone (1000–1550 km). Seismic paths from marsquakes and meteorite impacts traverse these layers (Fig. 1b), providing reliable constraints for each region (Supplementary Table 3). The analysis of P-wave spectra from distant events (see "Methods" and Supplementary Fig. 1) reveals that in the deep lithosphere, at depths of
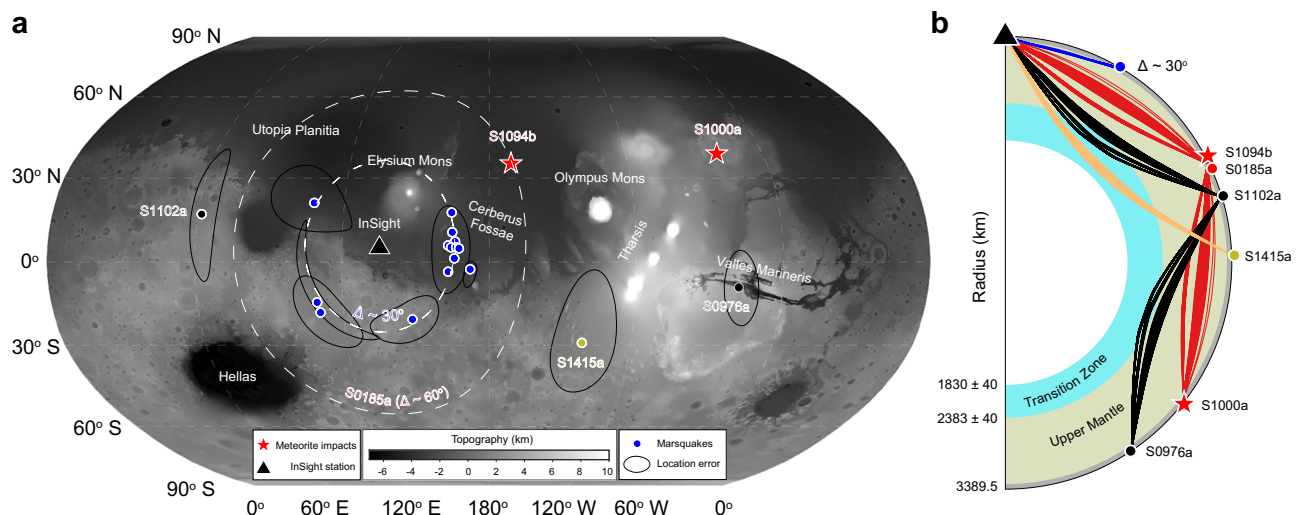
Fig. 1 | Geographical distribution of seismic events and meteorite impacts on Mars, and associated ray paths. a Topographic map of Mars[107] (MOLA) showing the epicenter locations of detected high-quality marsquakes (dots) and meteorite impacts (red stars) as recorded by InSight (black triangle). Black ellipses indicate the location uncertainties for each event. Dashed white curves represent epicentral distance contours at 30° and 60°. **b** Cross-section of Mars illustrating the seismic

wave propagation paths from selected events, including both marsquakes (in the crust or upper mantle) and meteorite impacts (at the surface). These ray paths traverse Mars' interior, extending from the upper mantle through the transition zone, and approaching the core-mantle boundary. The paths are calculated based on 1000 possible mantle models from body wave inversions[85].
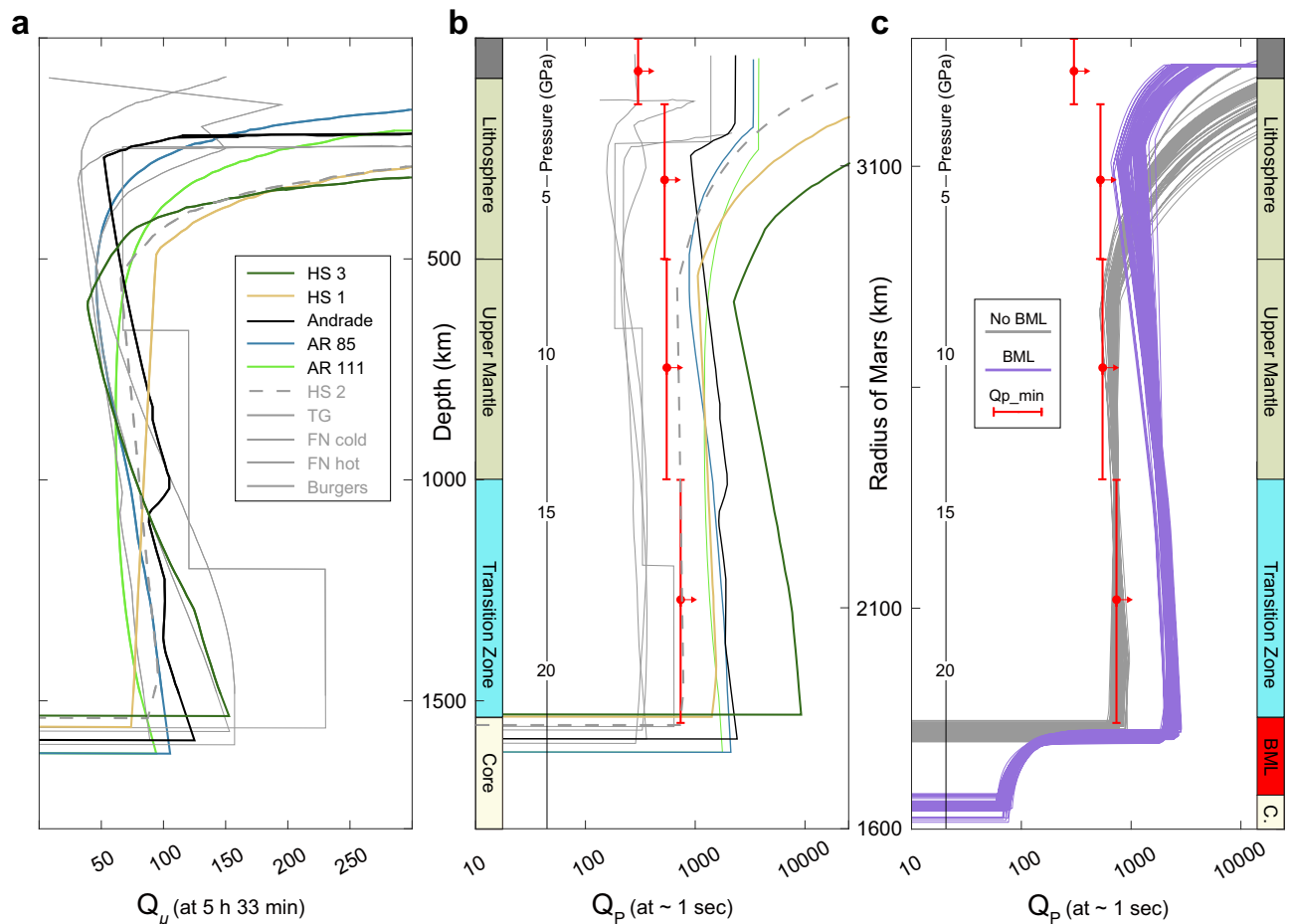
Fig. 2 | Attenuation profiles of Mars derived from tidal and seismic constraints.
a Shear attenuation $Q_\mu(r)$ profiles at Phobos tidal period of 5 h 33 min for ten mantle models (details of those models are summarized in Supplementary Table 1).
b P-wave attenuation $Q_P(r)$ profiles converted and extrapolated from the shear attenuation $Q_\mu(r)$ profiles at the tidal period (5 h 33 min) in (**a**) to a seismic period of ~1 s (see "Methods"). Red arrows indicate the seismically constrained minimum $Q_P(r)$ values at each depth range determined in this study, whereas gray lines represent models (i.e., the strong attenuation group) excluded due to their incompatibility with these minimum $Q_P(r)$ values. **c** Profiles of $Q_P(r)$ for the HS 2 model (dashed gray curve in (**b**)), comparing scenarios with (purple) and without (gray) a basal mantle layer (BML).

150–500 km (corresponding to about 2–6 GPa for Mars), the minimum $Q_P(r)$ value is 638 ± 124. Beneath the lithosphere, at depths of 500−1000 km (about 6−13 GPa for Mars), the minimum $Q_P(r)$ remains 612 ± 11. In the transition zone, at depths of 1000−1500 km (about 13−20 GPa for Mars), the minimum $Q_P(r)$ slightly increases to 746 ± 6 (Fig. 2b). This four-region division is primarily guided by the seismic ray coverage of events (Supplementary Fig. 2), and alternative partitioning schemes do not affect the main conclusion (Supplementary Fig. 3).

These lower bounds for $Q_P(r)$ clearly favor the "weak attenuation" models (e.g., HS1, HS3, Andrade, AR 85, and AR 111, see Supplementary Table 1 for details of those models), as this model group aligns more closely with the minimum $Q_P(r)$ values derived from deep-penetrating seismic waves. This suggests that weak attenuation is the most plausible representation of Mars' deep mantle properties (150–1500 km). Previous studies have identified weak attenuation of Mars within the lithosphere up to ~ 200 km[20,21]. Taken together, Mars' crust, upper mantle, and transition zone all likely exhibit weak attenuation.

To further evaluate the differences in seismic attenuation between Mars and Earth, we adapted Earth's PREM model to Martian conditions by accounting for differences in pressure, temperature, and seismic period (see "Methods"). The modified PREM model predicts a much more rapid high-frequency decay in the P-wave spectrum than observations on Mars, even before accounting for additional decay from source effects and scattering (Fig. 3). This discrepancy indicates that Mars' mantle is significantly less

attenuating than Earth's and points to fundamental differences in grain size, water content, oxygen fugacity, and/or temperature.

Discussion
Comparative attenuation between Mars and Earth
Understanding the differences and similarities between Earth and Mars is essential for unraveling planetary formation, evolution, and habitability. It has been a long-standing idea that Mars may have been richer in water than Earth due to accreting materials at larger distance to the sun[1]. However, recent studies challenge this idea by suggesting that Earth and Mars may share a genetic link[2]. These studies propose that the building blocks of Earth and Mars originated from similar sources, with a shared composition of up to 80–93%. Whether Mars was initially water-rich or water-poor compared to Earth, and whether it retains that state today, remains an open question.

On Earth, the mantle transition zone is considered as a major deep-water reservoir[22,23], as its dominant minerals, wadsleyite and ringwoodite, can contain more than 1 wt% water[49–51]. Given the iron-rich composition of the Martian mantle, both the upper mantle and transition zone of Mars could host a substantial water reservoir[25]. However, determining the exact water content in Mars' deep interior is challenging. Nevertheless, comparing Mars' attenuation profile with that of the Earth offers a means of estimating its relative water content—an approach similar to that applied to the Moon[52].
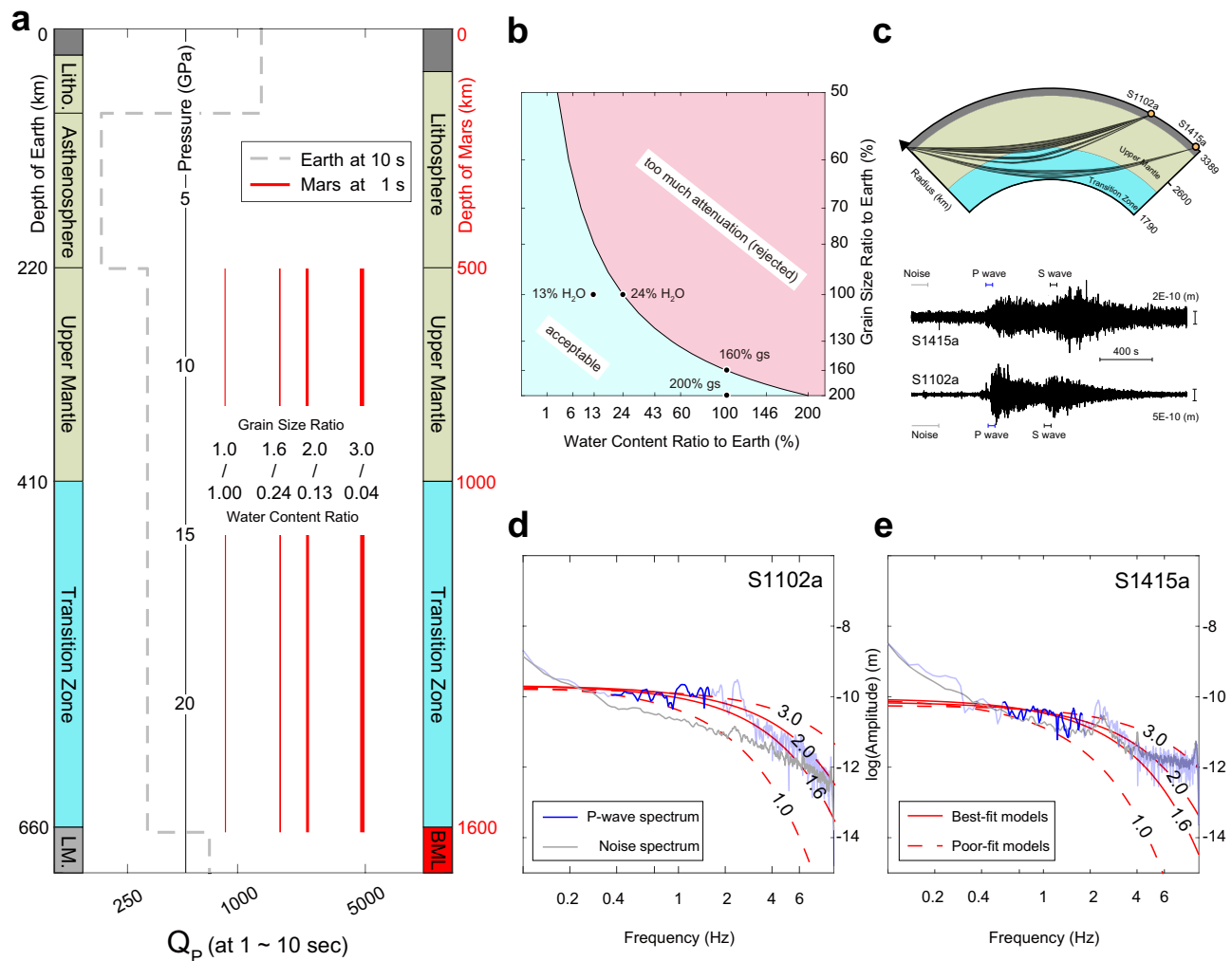
Fig. 3 | Comparative analysis of P-wave attenuation on Mars and Earth, and marsquake spectra. a P-wave attenuation $Q_P(r)$ profiles for Earth and Mars. The Earth profile (dashed gray line) is derived from the Preliminary Reference Earth Model[53] (PREM) at intermediate periods[100] (>10 s). Mars' profiles (solid red lines) represent attenuation profiles at a short period (1 s), corresponding to different grain size ratios between Mars and Earth (1.0, 1.6, 2.0, 3.0; from left to right) or their equivalent water content ratios (100%, 24%, 13%, 4%). Mars' profiles are calculated based on Earth's PREM model, with corrections to account for differences in period, temperature, and pressure (see "Methods"). **b** Grid search results for Mars from various combinations of water content ratios and grain size ratios relative to Earth. Models within the red-filled region exhibit excessive attenuation compared to the observed marsquake spectra shown in (**d**, **e**) and are thus rejected, either due to small grain sizes or high water content. **c** Cross-section (upper panel) of Mars highlighting the seismic ray paths for marsquakes S1102a and S1415a, with their maximum penetration depths into the upper mantle and transition zone. The paths are calculated based on 1000 mantle models[85]. Waveforms (lower panel) for marsquakes S1415a and S1102a. **d** Spectral analysis for marsquake S1102a. The logarithm of the waveform amplitude is plotted against frequency. The dark blue curve represents the P-wave spectrum used for fitting, and the light blue curve shows data excluded due to smaller amplitude or site amplification effects (see "Methods"). The gray curve indicates noise levels. The red synthetic curves correspond to the $Q_P(r)$ profiles of Mars shown in (**a**), with grain size ratios of 1.0, 1.6, 2.0, and 3.0 assuming the same water content (or equivalent to water content ratios of 100%, 24%, 13%, and 4% assuming the same grain size), and solid curves indicate the best-fitting models. **e** Similar spectral analysis for marsquake S1415a, following the same framework as (**d**).

Seismic attenuation on Earth has been extensively studied for over a century[31,32]. The globally averaged attenuation profile of Earth, as established in the Preliminary Reference Earth Model[53] (PREM), reveals distinct features: weak attenuation occurs in the lower mantle and the crust, strong attenuation in the asthenosphere, and intermediate attenuation in the rest of the upper mantle.

To compare seismic attenuation between the Earth and Mars, we began with the PREM model for Earth, and then applied corrections for differences in temperature, pressure, and seismic periods (10 s for Earth and 1 s for Mars) (see "Methods"). Previous studies indicate that Earth and Mars share similar potential temperatures of ~1600 K[25,40,54], therefore, seismic attenuation (quantified by $Q_P(r)$ values) in Mars is mostly influenced by grain size and water content. Larger grain sizes or lower water content increase $Q_P(r)$, and vice versa.

We systematically explored these effects by fixing one variable while varying the other.

Assuming Mars's grain size matches Earth's, models suggest that Mars's water content is approximately 13–24% of Earth's to reproduce the observed P-wave spectrum (Fig. 3d, e). This value is likely to overestimate intrinsic attenuation due to unmodeled scattering and source effects, leading to underestimated $Q_P(r)$ values. Consequently, assuming similar grain sizes, the actual water content in Mars' mantle must be further below this upper bound ratio of 13–24% to Earth's.

Alternatively, if Mars's water content equals Earth's, the minimum grain size required to match the observed P-wave spectrum is 1.6–2.0 times larger than Earth's. Grain size evolution reflects the dynamic balance between growth and comminution processes. While progressive grain growth is thermally enhanced, dislocation creep conversely drives size

reduction, with deformation intensity dictating its rate[55]. Mars' potential temperature may approximate Earth's values[40], yet its less vigorous mantle convection[55-59] promotes grain growth. Another key distinction from Earth is the absence of phase transitions from ringwoodite to bridgmanite and ferropericlase in Mars' interior. The lack of such transition suppresses recrystallization, thereby facilitating grain growth[40,60,61].

Distinguishing the relative effects of grain size and water content on seismic attenuation remains challenging, as both influence attenuation through the Maxwell timescale[62] (see "Methods"). This complexity is further compounded by experimental evidence demonstrating the impact of oxygen fugacity on seismic attenuation[63]. For example, like the effects from water, a lower oxygen fugacity can also decrease the attenuation.

Temperature exerts a strong control on attenuation[62]. Although previous studies suggest Earth and Mars share a similar potential temperature of ~1600 K[25,40,54], we consider a conservative uncertainty range of ±100 K to evaluate potential variations. Our analysis examines three potential temperatures (1500, 1600, and 1700 K; Supplementary Fig. 4), recalling that higher temperatures enhance attenuation. For Earth-like grain sizes, this favors a dry Martian mantle at moderate (1600 K) or high (1700 K) potential temperatures, while a cooler scenario (1500 K) could accommodate a wetter mantle.

Nevertheless, models assuming the same grain size, water content, oxygen fugacity, and temperature as Earth predict an excessively rapid high-frequency decay in the P-wave spectrum compared to observations, even without accounting for additional decay caused by source effects and scattering (Fig. 3). This suggests that Mars's mantle is significantly less attenuating than Earth's, pointing to fundamental differences in one or more of these factors. We also demonstrated that uncertainties in the shallow structure do not affect our conclusion of weak attenuation in deep Mars (see "Methods").

Reconciling tidal and seismic constraints

An important question arises as to why the "strong attenuation" group, inferred from tidal observations, fails to fit the seismic constraints. Recent seismological studies suggest the potential presence of a molten basal mantle layer (BML) at the core-mantle boundary (1550–1700 km)[64,65]. This BML is expected to exhibit strong attenuation, with a $Q_P(r)$ near 100 at the seismic period of 1 s[64], thereby significantly lowering the bulk Q_2 for Mars. Incorporating this layer into models could reconcile the apparent discrepancies between the seismic and tidal results. For instance, in the HS2 model set (Fig. 2c), the predicted $Q_P(r)$ in the depth range of 500−1500 km (about 6−20 GPa for Mars) is around 600–700, close to the lower bound of $Q_P(r)$ constrained by seismic observations. However, the existence of a molten BML with a $Q_P(r)$ of approximately 100 would increase the mantle $Q_P(r)$ to over 1000.

Therefore, when a BML is present, the mantle in the "strong attenuation" group transitions to a weakly attenuating state, aligning with seismic constraints that require low attenuation. In contrast, the "weak attenuation" group satisfies the seismic constraints regardless of whether a BML is present. Thus, our study does not point to a clear preference between homogeneous (without BML) or compositionally stratified (with BML) mantles.

Deep water within Mars

Seismic analyses reveal weak attenuation patterns in Mars' deep mantle (500–1500 km). However, further quantification of water content necessitates supplementary constraints on mineral grain size and thermal state. Assuming Earth-like mantle temperatures and grain sizes, Mars' upper mantle (500–1000 km depth) and transition zone (1000–1600 km depth) exhibit notable dryness, containing less than 13–24% of Earth's mantle water content. This dryness finds support in computational simulations demanding water-depleted mantle properties to replicate both the persistent volcanic activity and the observed tidal deformation[66,67]. This finding also aligns with studies on Martian meteorites documenting minimal water content (15–72 ppm) in mantle source regions[68], albeit potentially altered by secondary processes such as shock, degassing, or terrestrial contamination[25].

Two primary mechanisms could account for the low water content of the deep mantle. First, limited primordial water during accretion may have restricted the initial hydration state. Although the mantle has a substantial capacity to store water[25], this capacity is significantly lower than that of the overlying molten layer[69]. If a deep magma ocean once existed, water would have preferentially partitioned into melts within the BML and into the iron-rich core. As a result, any substantial deep-water reservoirs today would most likely be located at or below the core–mantle boundary. Second, inadequate water replenishment during planetary evolution may have contributed to the dryness of the mantle. Dynamic modeling indicates that partial melting and magmatic degassing could remove more than 80% of mantle water[70]. Additionally, the apparent absence of sustained plate tectonics—a longstanding scientific debate[71-76]—would have further restricted water transport from the surface to the deep mantle.

An alternative interpretation posits that lower mantle temperatures and/or larger grain sizes could accommodate the observed weak attenuation with water contents approaching terrestrial values. Mineral physics demonstrates that Mars' iron-rich mantle possesses greater water storage capacity than Earth's[25]. Such deep-water reservoirs could potentially sustain surface water features through magmatic degassing processes over geological timescales, with profound implications for Mars' hydrospheric evolution and potential habitability.

Conclusions

Previous studies of Mars' mantle have proposed both strong and weak attenuation models based on tidal observations. The seismic data from InSight's recordings of tectonic marsquakes and meteorite impacts now provide decisive new constraints, robustly favoring weak attenuation models. Our analysis reveals that within the 6–20 GPa pressure range, Mars' mantle (500–1500 km depth) displays systematically weaker attenuation than Earth's mantle (220–660 km depth). This difference likely results from a combination of factors, including lower water content, larger grain size, reduced oxygen fugacity, and/or lower temperatures.

When assuming Earth-like mantle temperatures and grain sizes, our findings indicate that Mars' upper mantle (500–1000 km) and transition zone (1000–1600 km) contain less than 13–24% of Earth's mantle water content. However, if Mars exhibits lower temperatures and/or larger grain sizes, its mantle water content could potentially match or even exceed terrestrial levels.

While this study provides important new constraints on the attenuation properties of the Martian mantle, it does not allow for a unique determination of the relative contributions of water content, grain size, and temperature. Definitive estimates of Mars' mantle water content require independent constraints on grain size and thermal structure. Future investigations targeting these parameters will be crucial for understanding the origin, transport, and long-term cycling of water on Mars. Such efforts may also help resolve the longstanding question of whether plate tectonics ever operated on Mars—an issue central to reconstructing the planet's geological, thermal, and habitability evolution.

Methods

Measuring seismic attenuation

In a heterogeneous medium, the displacement spectrum recorded at a receiver for a certain frequency f is influenced by several factors, including the propagation distance, the source rupture process, and the viscoelastic (i.e., intrinsic) attenuation and scattering effects along the path, and occasionally focusing/defocusing effects.

In a simplified scenario, where focusing and defocusing effects are neglected, the intrinsic attenuation and the scattering effects along the path can be characterized by the apparent quality factor, $\overline{Q_{apparent}}$. The amplitude spectrum $A(f)$ of the displacement can then be described by:

$$A(f) = A_0 \frac{1}{1 + \left(\frac{f}{f_c}\right)^\omega} \exp\left(-\pi f \frac{t}{\overline{Q_{apparent}}}\right) \quad (1)$$

where A_0 is the amplitude at long periods, incorporating geometrical spreading which is generally independent of frequency, f_c is the corner frequency of the source, ω is 2 for the Brune model[77] and can be larger than 2 for elongated faults[78], t is the propagation time of either the P or S wave, and $\overline{Q_{apparent}}$ is the average apparent quality factor along the propagation path.

The frequency-dependent amplitude decay is given by the ratio of the amplitude at a certain frequency to the long-period amplitude:

$$\frac{A(f)}{A_0} = \frac{1}{1+\left(\frac{f}{f_c}\right)^\omega} \exp\left(-\pi f \frac{t}{Q_{apparent}}\right) \qquad (2)$$

To fit this amplitude decay curve, we estimate two parameters: f_c and $\overline{Q_{apparent}}$. Consequently, there is an inherent tradeoff between these two parameters. However, if we deliberately disregard the source effects and focus solely on the path effects (i.e., attenuation and scattering) to fit the amplitude decay curve, we obtain a direct expression for the effective quality factor, $\overline{Q_{effective}}$, which is free from this tradeoff:

$$\frac{A(f)}{A_0} = \exp\left(-\pi f \frac{t}{Q_{effective}}\right) \qquad (3)$$

By comparing Eqs. (3) and (4), we find:

$$\frac{1}{\overline{Q_{effective}}} > \frac{1}{\overline{Q_{apparent}}} \qquad (4)$$

This indicates that the measured $\overline{Q_{effective}}$ value from the modeling in this study is smaller than $\overline{Q_{apparent}}$, making it a lower bound for $\overline{Q_{apparent}}$. Since the apparent quality factor $\overline{Q_{apparent}}$ reflects both intrinsic attenuation and scattering, and accurately separating $\overline{Q_{intrinsic}}$ from $\overline{Q_{scattering}}$ can be challenging, we focus on the lower limit of $\overline{Q_{intrinsic}}$, rather than its exact value.

The relationship between these quality factors is given by:

$$\frac{1}{\overline{Q_{apparent}}} = \frac{1}{\overline{Q_{intrinsic}}} + \frac{1}{\overline{Q_{scattering}}} \qquad (5)$$

Thus, the effective quality factor $\overline{Q_{effective}}$ measured in this study satisfies:

$$\frac{1}{\overline{Q_{effective}}} > \frac{1}{\overline{Q_{apparent}}} > \frac{1}{\overline{Q_{intrinsic}}} \qquad (6)$$

This confirms that the measured $\overline{Q_{effective}}$ value serves as a lower limit not only for $\overline{Q_{apparent}}$ but also for $\overline{Q_{intrinsic}}$.

Frequency-dependent attenuation at tidal and seismic periods
Attenuation in a medium is quantified by the quality factor Q and the number of cycles completed during the propagation time. At a given frequency, a high Q signifies low attenuation. In contrast, higher frequencies experience greater attenuation than lower frequencies, assuming the same Q and propagation distance, due to the increased number of cycles.

The quality factor Q is frequency-dependent and is often described by the relationship:

$$Q(f) = Q_0\left(\frac{f}{f_0}\right)^\alpha \qquad (7)$$

where $Q(f)$ is the quality factor at frequency $Q(f)$, Q_0 is the quality factor at the reference frequency f_0, and α is typically less than 1.0[79].

In the frequency range of seismic body waves (P and S waves) on Mars, approximately 0.5–1.5 Hz, Q can be approximated as constant. However, at the tidal period of 5 h and 33 min (corresponding to a frequency of 0.0005 Hz), Q can be up to ten times lower than the values observed at

seismic periods. Detailed conversions of Q values from tidal to seismic periods can be found in previous study[38].

Note that, in this study, the bulk modulus attenuation is neglected[80]. Therefore, the shear wave attenuation Q_S is equivalent to Q_μ, and the compressional wave attenuation Q_P is expressed as[62]:

$$Q_P = \frac{3V_P^2}{4V_S^2}Q_S \approx \frac{9}{4}Q_S \qquad (8)$$

Averaged attenuation along the seismic raypath
To estimate the averaged quality factor along the seismic path, $\overline{Q_{effective}}$, we utilized the arrival times of P and S waves provided by the catalog[44,81] and conducted a grid search for $\overline{Q_{effective}}$ values ranging from 10^2 to 10^5, with an exponent interval of 0.1. For each $\overline{Q_{effective}}$ value, we calculated the synthetic amplitude ratio using Eq. (3) and then computed the L2-norm between the synthetic and observed amplitude ratios.

We compare only the reliable portions of the marsquake spectrum, represented by the dark blue curve in Fig. 3d, e. Excluded regions include frequencies where the Marsquake spectrum falls below the noise spectrum, as well as higher frequencies (>1.8 Hz) affected by site amplification effects[82,83], which are not accounted for in the synthetic spectrum modeling.

The $\overline{Q_{effective}}$ value that minimized the misfit was identified as the best fit and is marked by the blue star in Supplementary Figs. 1 and 5 for P and S waves, respectively. To determine a range of acceptable $\overline{Q_{effective}}$ values, we established thresholds corresponding to 1.2–1.8 times the minimum misfit. For each threshold, we computed the mean and standard deviation of the $\overline{Q_{effective}}$ values that fell within this range. The mean value minus one standard deviation from this series is adopted as the final $\overline{Q_{effective}}$, which also defines the lower limit for $\overline{Q_{intrinsic}}$.

In addition to events clustering at an epicentral distance of ~30°, which primarily sample the uppermost mantle (<200 km), we also examined more distant events with ray paths that penetrate into deeper regions of the mantle (200–1300 km). These distant events provide valuable constraints on attenuation at greater depths, complementing the information obtained from the closer events. Together, these two groups of events (i.e., at ~30° and at greater distances) serve as representative cases that capture the range of ray path geometries and sampling depths.

The path-averaged values of $Q_{effective}$ for these representative events are summarized in Supplementary Table 2, showing variations in attenuation across different regions of Mars' mantle. Here, we focus on P waves rather than S waves because low-velocity zones in the S-wave velocity model led to greater variability and less predictable ray paths for S waves compared to P waves[84].

Note that for events S1102a (at ~73°) and S0976a (at ~146°), the travel distance for S1102a is approximately half that of S0976a. However, the penetration depths of the P wave for S1102a and the PP wave for S0976a are nearly identical due to the similar ray paths of the P and PP phases. Here, we select S1102a as the example event for this depth because it exhibits a larger $\overline{Q_{effective}}$ compared with S0976a. To constrain the lower limit of Q, we adopt the larger $\overline{Q_{effective}}$ value from S1102a, as it also satisfies the constraints imposed by S0976a. In contrast, choosing the smaller $\overline{Q_{effective}}$ value from S0976a would fail to meet the constraints of S1102a.

Lower limit of intrinsic Q at different depths
After obtaining the average effective Q values along the seismic paths, we further converted the path-averaged effective Q ($\overline{Q_{effective}}$, which also represents the lower limit of intrinsic Q along the seismic path) into the lower limit of the intrinsic Q at different depths.

Given the limited number of representative events listed in Supplementary Table 2, we divided the model into four regions and assumed constant Q values in each layer. These regions include upper lithosphere (0–150 km), lower lithosphere (150–500 km), upper mantle (500–1000 km), and the mantle transition zone (1000–1550 km).

This division is primarily guided by the current ray coverage of marsquakes (Supplementary Fig. 2), which samples the subsurface in four distinct regions. Further subdivisions would exceed the resolution provided by the available seismic data, making additional layers unconstrained. Thus, this approach is not arbitrary but rather reflects the coverages of the existing ray path from the events.

Moreover, this four-region division provides a first-order 1D attenuation profile for Mars. Notably, even the PREM—despite relying on far more extensive seismic data—also uses a layered Q structure. This suggests that our parameterization is not an oversimplification and is consistent with standard practice.

We have quantified the effects of alternative divisions. For instance, when splitting the regions 150–500 km and 500–1000 km into 150–750 km and 750–1000 km, the resulting minimum Q values shift slightly but still favor weakly attenuating (high-Q) models, leaving our conclusions unaffected (Supplementary Fig. 3).

For events clustering at ~30° (e.g., S1133c, with penetration depths of 127 ± 7 km), the seismic paths primarily travel through the upper lithosphere (0–150 km, UL):

$$t^*_{S1133c} = \frac{t_{S1133c,UL}}{Q_{effective,UL}} > \frac{t_{S1133c,UL}}{Q_{intrinsic,UL}} \tag{9}$$

Thus, the lower limit for the intrinsic Q in the upper lithosphere is:

$$\overline{Q_{intrinsic,UL}} > \frac{t_{S1133c,UL}}{t^*_{S1133c}} \tag{10}$$

For events S1094b and S1000a (with penetration depths of 464 ± 82 km and 530 ± 126 km, respectively), the seismic paths span both the upper lithosphere (0–150 km, UL) and the lower lithosphere (150–500 km, LL):

$$t^*_{S1094b} = \frac{t_{S1094b,UL}}{Q_{effective,UL}} + \frac{t_{S1094b,LL}}{Q_{effective,LL}} > \frac{t_{S1094b,UL}}{Q_{intrinsic,UL}} + \frac{t_{S1094b,LL}}{Q_{intrinsic,LL}} > \frac{t_{S1094b,LL}}{Q_{intrinsic,LL}} \tag{11}$$

From this, we derive:

$$\overline{Q_{intrinsic,LL}} > \frac{t_{S1094b,LL}}{t^*_{S1094b}} \tag{12}$$

Similarly, for the upper lithosphere:

$$\overline{Q_{intrinsic,UL}} > \frac{t_{S1094b,UL}}{t^*_{S1094b}} \tag{13}$$

For event S1102a (penetration depths of 1032 ± 111 km), the seismic paths extend into the upper lithosphere (0–150 km, UL), the lower lithosphere (150–500 km, LL), and the upper mantle (500–1000 km, UM).

For event S1415a (penetration depths of 1353 ± 33 km), the seismic paths traverse all four layers, including the transition zone (1000–1500 km, TZ).

Following similar analyses, we derived the lower limits of intrinsic Q for all four layers using the representative events:

$$\overline{Q_{intrinsic,UL}} > \max\left(\frac{t_{S1133c,UL}}{t^*_{S1133c}}, \frac{t_{S1094b,UL}}{t^*_{S1094b}}, \frac{t_{S1000a,UL}}{t^*_{S1000a}}, \frac{t_{S1102a,UL}}{t^*_{S1102a}}, \frac{t_{S1415a,UL}}{t^*_{S1415a}}\right) \tag{14}$$

$$\overline{Q_{intrinsic,LL}} > \max\left(\frac{t_{S1094b,LL}}{t^*_{S1094b}}, \frac{t_{S1000a,LL}}{t^*_{S1000a}}, \frac{t_{S1102a,LL}}{t^*_{S1102a}}, \frac{t_{S1415a,LL}}{t^*_{S1415a}}\right) \tag{15}$$

$$\overline{Q_{intrinsic,UM}} > \max\left(\frac{t_{S1102a,UM}}{t^*_{S1102a}}, \frac{t_{S1415a,UM}}{t^*_{S1415a}}\right) \tag{16}$$

$$\overline{Q_{intrinsic,TZ}} > \max\left(\frac{t_{S1415a,TZ}}{t^*_{S1415a}}\right) \tag{17}$$

The estimation of seismic paths and the corresponding uncertainties depends on both the event distance and the velocity model. In this study, we used 1000 seismic velocity models from body wave inversion results[85]. For each model, we varied the focal depth from 0 to 50 km and adjusted the epicentral distance based on the location error bars in the catalog[44].

Supplementary Table 3 presents the lower limits of intrinsic Q in all four layers: 306 ± 3 for the upper lithosphere (0–150 km), 638 ± 124 for the lower lithosphere (150–500 km), 612 ± 11 for the upper mantle (500–1000 km), and 746 ± 6 for the mantle transition zone (1000–1550 km).

Comparison of water content and grain size between Mars and Earth

To investigate differences in water content and grain size between Mars and Earth through seismic attenuation, we accounted for the effects of temperature, pressure, and frequency on attenuation in the two planets. In torsional forced oscillation experiments, the relationship between stress (σ) and strain (ε) is written as:

$$\varepsilon = J^*(f)\sigma = [J_1(f) + iJ_2(f)]\sigma \tag{18}$$

where $J^*(f)$ is the frequency (f) dependent complex compliance[62,86], and i denotes the imaginary unit. The shear quality factor, Q_μ is then given by:

$$Q_\mu(f) = \frac{J_1(f)}{J_2(f)} \tag{19}$$

Since $J^*(f)$ is dependent on frequency, composition, temperature, pressure, grain size, water content, and partial melting[62], the shear attenuation is also affected by those factors. However, the influence of composition on attenuation is likely small[87]. When the temperature is much lower than the solidus[88], which would likely be true around the mantle transition zone, the Q_μ dependence can be simplified and characterized by only two factors: frequency and the Maxwell timescale (τ_M), which is expressed as:

$$\tau_M = \frac{\eta}{\mu} \tag{20}$$

where μ is the shear modulus, and η is the diffusion creep viscosity[62]. In the absence of partial melting, the viscosity is expressed as:

$$\eta = A d^m (H_2O)^{-r} \exp\left(\frac{E + PV}{RT}\right) \tag{21}$$

where A is a pre-factor; d is the grain size; H_2O is the water content; T and P are temperature and pressure; E and V are activation energy and activation volume; and R is the gas constant[89]. For diffusion creep, m and r are set to 3 and 1, respectively[89].

To quantify the effects of grain size and water content, the temperature (or temperature differences) between Earth and Mars must be considered. Previous studies indicate that Earth and Mars have similar potential temperatures of ~1600 K[25,40,54]. Here, we independently estimate the temperature difference ($\triangle T$) between Earth and Mars based on their compressional velocity differences ($\triangle V_P$):

$$\triangle V_P = \triangle V_P^C + \frac{\partial V_P}{\partial T} \triangle T \tag{22}$$

where $\triangle V_P^C$ characterizes the velocity difference due to the compositional difference, and $\partial V_P / \partial T$ is the temperature gradient of V_P.

We determined $\triangle V_P^C$ by calculating the velocity differences using Perple_X[90,91] based on the Earth's primitive mantle composition[92] and the Mars' mantle composition[93] along the Mars' geotherm[54].

For the selection of the Martian mantle composition model, we evaluated six options[93–98]. Ultimately, we selected the model[93], which best aligns with the triplication observations reported by previous study[54].

The temperature gradient, $\partial V_P / \partial T$, was estimated by calculating the V_P difference between 50 K above and 50 K below the Mars' geotherm, divided by 100 K[90,91]. Mars is found to be only 30 K hotter than Earth near the mantle transition zone region, broadly consistent with a similar potential temperature previous study suggested. Depths on Mars and Earth were converted to pressure using the relationships in previous studies[54,99]. Assuming PREM attenuation structure represents a 0.1 Hz frequency[100] and following attenuation models from previous study[62], we calculated the expected τ_M at 310 and 500 km depths on Earth using the Very Boradband Rheology calculator[101]. These depths correspond to the midpoints of the upper mantle layer (220–400 km) and the mantle transition zone layer (400–600 km), respectively.

To estimate τ_M for Mars at 815 and 1362 km depths (the pressure condition is corresponding to 310 and 500 km depths on Earth), we adjusted the temperature difference between the two planets in the viscosity Arrhenius term. Then, after converting the frequency from 0.1 to 1 Hz, we obtained the expected seismic Q_P profile for Mars[101] (assuming the same grain size and water content as Earth's PREM, after corrections for differences in temperature and frequency).

Note that we assumed a 0.1 Hz frequency for PREM based on observations showing attenuation is approximately constant between 0.001 and 0.1 Hz[100]. This behavior is also consistent with the absorption band in previous study[62] for this determined τ_M.

Based on this expected Q_P profile for Mars, we generated a range of candidate Q_P profiles by varying grain size or water content (Eq. 21). We then tested which profiles could explain the recorded P-wave spectrum.

Since grain size (d) and water content (H_2O) would influence attenuation through τ_M, changes in d^3 are mathematically equivalent to changes in H_2O^{-1}. As a result, for a certain temperature, we cannot fully distinguish between the two factors. Therefore, we considered both possibilities for the discussions.

Given the strong influence of temperature on attenuation and the uncertainties in estimating Mars' interior temperature in both this study and previous work, we considered a conservatively large uncertainty of ±100 K. We evaluated three potential temperatures: 1500, 1600, and 1700 K (Supplementary Fig. 4). Higher temperatures increase attenuation, so a dry Martian mantle is favored if the potential temperature is moderate (1600 K) or high (1700 K), assuming Earth-like grain sizes. In contrast, a cooler potential temperature (1500 K) permits a wetter mantle scenario.

Modeling marsquake spectrum using attenuation model

To simulate the event spectrum based on the attenuation model of Mars, the process involves two steps. The first step is to construct the attenuation model of Mars using Earth's PREM model as a reference (discussed in the above section). The second step is to simulate the seismic spectrum based on this Mars-specific attenuation model using Eq. (3).

In the first step, a critical consideration is how uncertainties in the shallow structure influence our analysis of the deep mantle. Specifically, for Earth, weak attenuation is observed in the lower mantle and crust, strong attenuation in the asthenosphere, and intermediate attenuation levels in the remainder of the upper mantle. However, for Mars, there are two major differences. First, there is no clear evidence for the presence of an asthenosphere[84], as well as associated partial melting[102]. Second, the exact attenuation properties of the shallow layers (0–150 km) remain unknown. These differences must be accounted for when adapting Earth's attenuation model to Mars.

To address these challenges, we apply the effective Q values (converted from Earth's PREM) at depths greater than 500 km. For the two shallower regions—specifically, the upper lithosphere (0–150 km) and the zone corresponding to Earth's asthenosphere (150–500 km)—we set the effective Q values to infinity and adopt values representative of the upper mantle (500–1000 km) to those two regions, respectively. We did not consider the presence of a highly attenuating asthenosphere[103]. By doing so, we intentionally overestimate the Q values in the shallow regions (i.e., underestimate the intrinsic attenuation effects). If such a layer exists on Mars, it would significantly contribute to the total attenuation, likely to further reduce the already weak attenuation in the deeper mantle.

This underestimation of intrinsic attenuation serves as a practical approach to account for the influence of shallow structures on deeper regions. Although we cannot eliminate this influence, we can demonstrate that the uncertainty in the shallow parts (or the underestimation of attenuation in these regions) does not affect our conclusion that Mars exhibits weak attenuation. This strategy is analogous to our approach of underestimating intrinsic attenuation by intentionally neglecting effects related to scattering and source corner frequency.

Despite these systematic underestimations, the constructed attenuation model for Mars still exhibits significantly greater spectral decay compared to observations from recorded marsquakes (e.g., S1102a and S1415a, in Fig. 3). This discrepancy implies that the constructed Mars' mantle model demonstrates weaker attenuation than Earth's. Given the deliberate underestimations, the actual attenuation in Mars' deep mantle is likely even weaker, reinforcing our conclusion.

Data availability

The seismic catalog of Marsquake Service is described by the InSight Marsquake Service[104]. Arrival times and underlying data are provided with this paper and by the InSight Marsquake Service Team[44,81]. The raw and processed data used in the analysis and to reproduce the figures are available on the Zenodo repository at https://doi.org/10.5281/zenodo.14759243[105].

Code availability

All the computations made in this article are either described in the method sections or based on codes described in published papers that are cited in the reference list. The Perple_X code[90] is available at https://www.perplex.ethz.ch. The codes used in the analysis and to make the figures are available on the Zenodo repository at https://doi.org/10.5281/zenodo.14759265[106].

References

1. Brasser, R. The formation of Mars: building blocks and accretion time scale. *Space Sci. Rev.* **174**, 11–25 (2013).
2. Fitoussi, C., Bourdon, B. & Wang, X. The building blocks of Earth and Mars: a close genetic link. *Earth Planet. Sci. Lett.* **434**, 151–160 (2016).
3. Shizgal, B. D. & Arkos, G. G. Nonthermal escape of the atmospheres of Venus, Earth, and Mars. *Rev. Geophys.* **34**, 483–505 (1996).
4. Langlais, B., Purucker, M. E., & Mandea, M. Crustal magnetic field of Mars. *J.Geophys. Res. Planets* **109**, E02008 (2004).
5. Ruiz, J. et al. The thermal evolution of Mars as constrained by paleo-heat flows. *Icarus* **215**, 508–517 (2011).
6. Sandu, C., & Kiefer, W. S. Degassing history of Mars and the lifespan of its magnetic dynamo. *Geophys. Res. Lett.* **39**, L03201 (2012).
7. Scheller, E. L., Ehlmann, B. L., Hu, R., Adams, D. J. & Yung, Y. L. Long-term drying of Mars by sequestration of ocean-scale volumes of water in the crust. *Science* **372**, 56–62 (2021).
8. Hernández-Montenegro, J. D., Asimow, P. D. & Herzberg, C. T. Estimating primary magmas from Mars with PRIMARSMELT: implications for the petrogenesis of some Martian rocks and the thermal evolution of Mars. *J. Geophys. Res. Planets* **129**, e2024JE008508 (2024).

9. Greeley, R. & Schneid, B. D. Magma generation on Mars: amounts, rates, and comparisons with Earth, Moon, and Venus. *Science* **254**, 996–998 (1991).

10. Carr, M. H. & Head, J. W. Martian surface/near-surface water inventory: Sources, sinks, and changes with time. *Geophys. Res. Lett.* **42**, 726–732 (2015).

11. Jakosky, B. M. & Hallis, L. J. Fate of an earth-like water inventory on Mars. *J. Geophys. Res. Planets* **129**, e2023JE008159 (2024).

12. Sori, M. M. & Bramson, A. M. Water on Mars, with a grain of salt: local heat anomalies are required for basal melting of ice at the south pole today. *Geophys. Res. Lett.* **46**, 1222–1231 (2019).

13. Morgan, G. A. et al. Availability of subsurface water-ice resources in the northern mid-latitudes of Mars. *Nat. Astron.* **5**, 230–236 (2021).

14. Posiolova, L. et al. Largest recent impact craters on Mars: orbital imaging and surface seismic co-investigation. *Science* **378**, 412–417 (2022).

15. Ehlmann, B. L., Mustard, J. F. & Murchie, S. L. Geologic setting of serpentine deposits on Mars. *Geophys. Res. Lett.* **37**, L06201 (2010).

16. Liu, Y. et al. Zhurong reveals recent aqueous activities in Utopia Planitia, Mars. *Sci. Adv.* **8**, eabn8555 (2022).

17. Tutolo, B. M. & Tosca, N. J. Observational constraints on the process and products of Martian serpentinization. *Sci. Adv.* **9**, eadd8472 (2023).

18. Banerdt, W. B. et al. Initial results from the InSight mission on Mars. *Nat. Geosci.* **13**, 183–189 (2020).

19. Wright, V., Morzfeld, M. & Manga, M. Liquid water in the Martian mid-crust. *Proc. Natl. Acad. Sci. USA* **121**, e2409983121 (2024).

20. Lognonné, P., Banerdt, W. B., Pike, W. T., Giardini, D. & Zweifel, P. Constraints on the shallow elastic and anelastic structure of Mars from InSight seismic data. *Nat. Geosci.* **13**, 213–220 (2020).

21. Menina, S. et al. Energy envelope and attenuation characteristics of high-frequency (HF) and very-high-frequency (VF) Martian events. *Bull. Seismol. Soc. Am.* **111**, 3016–3034 (2021).

22. Bercovici, D. & Karato, S. I. Whole-mantle convection and the transition-zone water filter. *Nature* **425**, 39–44 (2003).

23. Fei, H. et al. A nearly water-saturated mantle transition zone inferred from mineral viscosity. *Sci. Adv.* **3**, e1603024 (2017).

24. Van Keken, P. E., Hacker, B. R., Syracuse, E. M., & Abers, G. A. Subduction factory: 4. Depth-dependent flux of H_2O from subducting slabs worldwide. *J. Geophys. Res. Solid Earth* **116**, (2011).

25. Dong, J. et al. Water storage capacity of the Martian mantle through time. *Icarus* **385**, 115113 (2022).

26. Lognonné, P. & Mosser, B. Planetary seismology. *Surv. Geophys.* **14**, 239–302 (1993).

27. Karato, S. I. Mapping water content in upper mantle. *Geophys. Monogr. Am. Geophys. Union* **138**, 135–152 (2003).

28. Abers, G. A. et al. Reconciling mantle attenuation-temperature relationships from seismology, petrology, and laboratory measurements. *Geochem. Geophys. Geosyst.* **15**, 3521–3542 (2014).

29. Romanowicz, B. & Mitchell, B. 1.25—deep earth structure: Q of the Earth from crust to core. *Treatise Geophys.* **1**, 789–827 (2015).

30. Talavera-Soza, S., Cobden, L., Faul, U. H., & Deuss, A. Global 3D model of mantle attenuation using seismic normal modes. *Nature* **637**, 1131–1135 (2025).

31. Angenheister, G. Bestimmung der Fortpflanzungsgeschwindigkeit und Absorption von Erdbebenwellen, die durch den Gegenpunkt des Herdes gegangen sind. Mit 1 Tafel. *Nachr. von Ges. Wiss. Gött. Math. Phys. Kl.* **1906**, 110–120 (1906).

32. Gutenberg, B. Dispersion und Extinktion von seismischen Oberflchenwellen und der Aufbau der obersten Erdschichten. *Phys. Z.* **25**, 377–382 (1924).

33. Redmond, J. C. & Fish, F. F. The luni-tidal interval in Mars and the secular acceleration of Phobos. *Icarus* **3**, 87–91 (1964).

34. MacDonald, G. J. Tidal friction. *Rev. Geophys.* **2**, 467–541 (1964).

35. Kaula, W. M. Tidal dissipation by solid friction and the resulting orbital evolution. *Rev. Geophys.* **2**, 661–685 (1964).

36. Bagheri, A., Khan, A., Al-Attar, D., Crawford, O. & Giardini, D. Tidal response of Mars constrained from laboratory-based viscoelastic dissipation models and geophysical data. *J. Geophys. Res. Planets* **124**, 2703–2727 (2019).

37. Samuel, H., Lognonné, P., Panning, M. & Lainey, V. The rheology and thermal history of Mars revealed by the orbital evolution of Phobos. *Nature* **569**, 523–527 (2019).

38. Pou, L. et al. Tidal constraints on the Martian interior. *J. Geophys. Res. Planets* **127**, e2022JE007291 (2022).

39. Bills, B. G., Neumann, G. A., Smith, D. E., & Zuber, M. T. Improved estimate of tidal dissipation within Mars from MOLA observations of the shadow of Phobos. *J. Geophys. Res. Planets* **110**, E07004 (2005).

40. Nimmo, F. & Faul, U. H. Dissipation at tidal and seismic frequencies in a melt-free, anhydrous Mars. *J. Geophys. Res. Planets* **118**, 2558–2569 (2013).

41. Latham, G. et al. Moonquakes. *Science* **174**, 687–692 (1971).

42. Nakamura, Y. Shallow moonquakes-How they compare with earthquakes. *Lunar Planet. Sci. Conf. Proc.* **11**, 1847–1853 (1980).

43. Giardini, D. et al. The seismicity of Mars. *Nat. Geosci.* **13**, 205–212 (2020).

44. Ceylan, S. et al. The marsquake catalogue from InSight, sols 0–1011. *Phys. Earth Planet. Inter.* **333**, 106943 (2022).

45. Zenhäusern, G. et al. An estimate of the impact rate on Mars from statistics of very-high-frequency marsquakes. *Nat. Astron.* **8**, 1138–1147 (2024).

46. Lognonné, P. et al. SEIS: Insight's seismic experiment for internal structure of Mars. *Space Sci. Rev.* **215**, 1–170 (2019).

47. Wang, Y. & Lawton, D. C. Time-lapse attenuation variations using distributed acoustic sensing vertical seismic profile data during CO_2 injection at CaMI Field Research Station. *Alta. Can. Geophys.* **89**, N31–N44 (2024).

48. Shearer, P. M. *Introduction to Seismology* (Cambridge University Press, 2019).

49. Huang, X., Xu, Y. & Karato, S. I. Water content in the transition zone from electrical conductivity of wadsleyite and ringwoodite. *Nature* **434**, 746–749 (2005).

50. Bolfan-Casanova, N. Water in the Earth's mantle. *Mineral. Mag.* **69**, 229–257 (2005).

51. Ohtani, E. Hydrous minerals and the storage of water in the deep mantle. *Chem. Geol.* **418**, 6–15 (2015).

52. Karato, S. I. Geophysical constraints on the water content of the lunar mantle and its implications for the origin of the Moon. *Earth Planet. Sci. Lett.* **384**, 144–153 (2013).

53. Dziewonski, A. M. & Anderson, D. L. Preliminary reference Earth model. *Phys. Earth Planet. Inter.* **25**, 297–356 (1981).

54. Huang, Q. et al. Seismic detection of a deep mantle discontinuity within Mars by InSight. *Proc. Natl. Acad. Sci. USA* **119**, e2204474119 (2022).

55. Austin, N. J. & Evans, B. Paleowattmeters: a scaling relation for dynamically recrystallized grain size. *Geology* **35**, 343–346 (2007).

56. Solomatov, V. S., & Reese, C. C. Grain size variations in the Earth's mantle and the evolution of primordial chemical heterogeneities. *J. Geophys. Res. Solid Earth* **113**, B07408 (2008).

57. Coltice, N., Gérault, M. & Ulvrová, M. A mantle convection perspective on global tectonics. *Earth Sci. Rev.* **165**, 120–150 (2017).

58. Day, J. M. et al. Martian magmatism from plume metasomatized mantle. *Nat. Commun.* **9**, 4799 (2018).

59. Schierjott, J. C., Thielmann, M., Rozel, A. B., Golabek, G. J. & Gerya, T. V. Can grain size reduction initiate transform faults?—insights from a 3-D numerical study. *Tectonics* **39**, e2019TC005793 (2020).

60. Karato, S. I. The role of recrystallization in the preferred orientation of olivine. *Phys. Earth Planet. Inter.* **51**, 107–122 (1988).

61. Demouchy, S. et al. Forsterite to wadsleyite phase transformation under shear stress and consequences for the Earth's mantle transition zone. *Phys. Earth Planet. Inter.* **184**, 91–104 (2011).

62. McCarthy, C., Takei, Y. & Hiraga, T. Experimental study of attenuation and dispersion over a broad frequency range: 2. The universal scaling of polycrystalline materials. *J. Geophys. Res. Solid Earth* **116**, B09207 (2011).

63. Cline Ii, C. J., Faul, U. H., David, E. C., Berry, A. J. & Jackson, I. Redox-influenced seismic properties of upper-mantle olivine. *Nature* **555**, 355–358 (2018).

64. Samuel, H. et al. Geophysical evidence for an enriched molten silicate layer above Mars's core. *Nature* **622**, 712–717 (2023).

65. Khan, A. et al. Evidence for a liquid silicate layer atop the Martian core. *Nature* **622**, 718–723 (2023).

66. Plesa, A. C. et al. The thermal state and interior structure of Mars. *Geophys. Res. Lett.* **45**, 12–198 (2018).

67. Thiriet, M., Michaut, C., Breuer, D. & Plesa, A. C. Hemispheric dichotomy in lithosphere thickness on Mars caused by differences in crustal structure and composition. *J. Geophys. Res. Planets* **123**, 823–848 (2018).

68. McCubbin, F. M. et al. Heterogeneous distribution of H_2O in the Martian interior: implications for the abundance of H_2O in depleted and enriched mantle sources. *Meteorit. Planet. Sci.* **51**, 2036–2060 (2016).

69. Li, Y., Vočadlo, L., Sun, T. & Brodholt, J. P. The Earth's core as a reservoir of water. *Nat. Geosci.* **13**, 453–458 (2020).

70. Fraeman, A. A. & Korenaga, J. The influence of mantle melting on the evolution of Mars. *Icarus* **210**, 43–57 (2010).

71. Sleep, N. H. Martian plate tectonics. *J. Geophys. Res. Planets* **99**, 5639–5655 (1994).

72. Frey, H. V., Roark, J. H., Shockey, K. M., Frey, E. L. & Sakimoto, S. E. Ancient lowlands on Mars. *Geophys. Res. Lett.* **29**, 22–1 (2002).

73. Breuer, D. & Spohn, T. Early plate tectonics versus single-plate tectonics on Mars: evidence from magnetic field history and crust evolution. *J. Geophys. Res. Planets* **108**, 5072 (2003).

74. Frey, H. V. Impact constraints on the age and origin of the lowlands of Mars. *Geophys. Res. Lett.* **33**, L08S02 (2006).

75. Baker, V. R., Maruyama, S. & Dohm, J. M. Tharsis superplume and the geological evolution of early Mars. in *Superplumes: Beyond Plate Tectonics* 507–522 (Springer, 2007).

76. Tosi, N. & Padovan, S. Mercury, Moon, Mars: surface expressions of mantle convection and interior evolution of stagnant-lid bodies. in *Mantle Convection and Surface Expressions* 455–489 (Wiley, 2021).

77. Brune, J. N. Tectonic stress and the spectra of seismic shear waves from earthquakes. *J. Geophys. Res.* **1896–1977**, 4997–5009 (1970).

78. Stähler, S. C. et al. Tectonics of Cerberus Fossae unveiled by Marsquakes. *Nat. Astron.* **6**, 1376–1386 (2022).

79. Cheng, H. X. & Kennett, B. L. N. Frequency dependence of seismic wave attenuation in the upper mantle beneath the Australian region. *Geophys. J. Int.* **150**, 45–57 (2002).

80. Anderson, D. L. & Hart, R. S. Q of the Earth. *J. Geophys. Res. Solid Earth* **83**, 5869–5882 (1978).

81. Clinton, J. F. et al. The Marsquake catalogue from InSight, sols 0–478. *Phys. Earth Planet. Inter.* **310**, 106595 (2021).

82. Hobiger, M. et al. The shallow structure of Mars at the InSight landing site from inversion of ambient vibrations. *Nat. Commun.* **12**, 6756 (2021).

83. Carrasco, S. et al. Empirical H/V spectral ratios at the InSight landing site and implications for the martian subsurface structure. *Geophys. J. Int.* **232**, 1293–1310 (2023).

84. Khan, A. et al. Upper mantle structure of Mars from InSight seismic data. *Science* **373**, 434–438 (2021).

85. Duran, C. et al. Seismology on Mars: an analysis of direct, reflected, and converted seismic body waves with implications for interior structure. *Phys. Earth Planet. Inter.* **325**, 106851 (2022).

86. Faul, U. H. & Jackson, I. The seismological signature of temperature and grain size variations in the upper mantle. *Earth Planet. Sci. Lett.* **234**, 119–134 (2005).

87. Shito, A., Karato, S. I., Matsukage, K. N. & Nishihara, Y. Towards mapping the three-dimensional distribution of water in the upper mantle from velocity and attenuation tomography. *Earth's. Deep Water Cycle* **168**, 225–236 (2006).

88. Yamauchi, H. & Takei, Y. Polycrystal anelasticity at near-solidus temperatures. *J. Geophys. Res. Solid Earth* **121**, 7790–7820 (2016).

89. Hirth, G. & Kohlstedt, D. Rheology of the upper mantle and the mantle wedge: a view from the experimentalists. *Geophys. Monogr. Am. Geophys. union* **138**, 83–106 (2003).

90. Connolly, J. A. D. The geodynamic equation of state: what and how. *Geochem. Geophys. Geosyst.* **10**, Q10014 (2009).

91. Stixrude, L. & Lithgow-Bertelloni, C. Thermodynamics of mantle minerals-II. Phase equilibria. *Geophys. J. Int.* **184**, 1180–1213 (2011).

92. McDonough, W. F. & Sun, S. S. The composition of the Earth. *Chem. Geol.* **120**, 223–253 (1995).

93. Yoshizaki, T. & McDonough, W. F. The composition of Mars. *Geochim. et Cosmochim. Acta* **273**, 137–162 (2020).

94. Dreibus, G. & Wanke, H. "Mars, a volatile-rich planet." Meteoritics **20**, 367–381 (1985).

95. Lodders, K. & Fegley, B. An oxygen isotope model for the composition of Mars. *Icarus* **126**, 373–394 (1997).

96. Khan, A. & Connolly, J. A. D. "Constraining the composition and thermal state of Mars from inversion of geophysical data." *J. Geophys. Res. Planets* **113**, E07003 (2008).

97. Taylor, G. J. The bulk composition of Mars. *Geochemistry* **73**, 401–420 (2013).

98. Sanloup, C., Jambon, A. & Gillet, P. A simple chondritic model of Mars. *Phys. Earth Planet. Inter.* **112**, 43–54 (1999).

99. Katsura, T. A revised adiabatic temperature profile for the mantle. *J. Geophys. Res. Solid Earth* **127**, e2021JB023562 (2022).

100. Warren, L. M. & Shearer, P. M. Investigating the frequency dependence of mantle Q by stacking P and PP spectra. *J. Geophys. Res. Solid Earth* **105**, 25391–25402 (2000).

101. Havlin, C., Holtzman, B. K. & Hopper, E. Inference of thermodynamic state in the asthenosphere from anelastic properties, with applications to North American upper mantle. *Phys. Earth Planet. Inter.* **314**, 106639 (2021).

102. Hua, J., Fischer, K. M., Becker, T. W., Gazel, E. & Hirth, G. Asthenospheric low-velocity zone consistent with globally prevalent partial melting. *Nat. Geosci.* **16**, 175–181 (2023).

103. Chantel, J. et al. Experimental evidence supports mantle partial melting in the asthenosphere. *Sci. Adv.* **2**, e1600246 (2016).

104. InSight Marsquake Service. Mars Seismic Catalogue, InSight Mission; V13 2023-01-01. ETHZ, IPGP, JPL, ICL, Univ. Bristol https://doi.org/10.12686/a19 (2023).

105. Li, J. Derived_data. Zenodo https://doi.org/10.5281/zenodo.14759243 (2025a).

106. Li, J. Derived_codes. Zenodo https://doi.org/10.5281/zenodo.14759265 (2025b).

107. Smith, D. E. et al. Mars orbiter laser altimeter: experiment summary after the first year of global mapping of Mars. *J. Geophys. Res. Planets* **106**, 23689–23722 (2001).

Acknowledgements

Author contributions

J.L. designed the research. J.L. wrote the main text, with inputs from J.H.,
T.P.F., L.A., L.P., Q.H., H.M., H.S., Z.J., W.W., T.Y., and T.Z. J.L. performed
research. J.H. wrote and contributed to the Methods section on attenuation
modeling. J.L., T.Z., Q.H., and H.M. wrote and contributed to the Methods
section on seismic analysis and inversion. All authors revised the
manuscripts.

Competing interests

The authors declare no competing interests.

Additional information

Supplementary information The online version contains
supplementary material available at
https://doi.org/10.1038/s43247-025-02664-9.

Correspondence and requests for materials should be addressed to
Jiaqi Li.

Peer review information *Communications Earth & Environment* thanks the
reviewer(s) for their contribution to the peer review of this work. Primary

handling editors: Renbiao Tao, Joe Aslin, and Alice Drinkwater. [A peer
review file is available.]

Reprints and permissions information is available at
http://www.nature.com/reprints

Publisher's note Springer Nature remains neutral with regard to
jurisdictional claims in published maps and institutional affiliations.